Infrared Physics & Technology 127 (2022) 104446

Contents lists available at ScienceDirect

Infrared Physics and Technology

journal homepage: www.elsevier.com/locate/infrared

Nanoindentation of $Hg_{0.7}Cd_{0.3}Se$ prepared by molecular beam epitaxy

Zekai Zhang, Wenwu Pan, Mariusz Martyniuk, Shuo Ma, Lorenzo Faraone, Wen Lei *

Department of Electrical, Electronic, and Computer Engineering, The University of Western Australia, Perth, WA 6009, Australia

ARTICLE INFO

Keywords:
HgCdSe
Young's modulus
Hardness
Nanoindentation

ABSTRACT

This paper presents a study of the mechanical properties of $Hg_{0.7}Cd_{0.3}Se$ grown via molecular beam epitaxy on GaSb (211)B substrates. By applying nanoindentation measurements, the statistical average values of Young's modulus and hardness of $Hg_{0.7}Cd_{0.3}Se$ extracted from corresponding 43 effective load–displacement curves are determined to be approximately 51 GPa with 7.4 GPa standard deviation and 0.93 GPa with 0.05 GPa standard deviation, respectively. In response to increasing loading force, $Hg_{0.7}Cd_{0.3}Se$ material is found to transition from purely elastic character to elasto-plastic behaviour, which is observed to be characterized by "pop-in" discontinuities in the recorded load-penetration curves and occurring at a shear stress of around 2.25 GPa. Compared to the mechanical properties of $Hg_{0.7}Cd_{0.3}Te$, $Hg_{0.7}Cd_{0.3}Se$ is found to present more favorable hardness and plastic threshold shear stress from the point of view of robustness for device fabrication processing and possible integration with MEMS technology.

1. Introduction

Over the past decades, mercury cadmium telluride (HgCdTe, MCT) infrared (IR) detectors fabricated using material grown on lattice-matched CdZnTe (CZT) substrates have dominated the high-performance market for IR imaging and sensing applications due to their outstanding optoelectronic performance [1–5]. However, HgCdTe IR technology based on CZT substrates suffers from limitations imposed by the substrate, resulting in high cost and small array format size that struggle to meet the requirements of broad market infrared applications. Although various alternative substrates were studied for growing high quality HgCdTe in order to lower the production cost and increase the array format size [6–9], high density of misfit dislocations were generated due to the large lattice mismatch between alternative substrates and HgCdTe which degraded the device performance. To address this challenge, mercury cadmium selenide (HgCdSe, MCS) has been proposed as an alternative IR material to HgCdTe. Recent research on the structural, electrical, and optical properties of HgCdSe materials grown by molecular beam epitaxy (MBE) [10–12], indicate comparable optoelectronic properties to HgCdTe in relation to IR detection. Most importantly, since HgCdSe is nearly lattice-matched to GaSb, the use of GaSb substrates offers larger wafer size and higher quality in comparison to CZT substrates [13]. Therefore, HgCdSe-based IR devices have a great potential for meeting the requirements of next generation infrared detectors with features of larger array format size and lower production cost [14]. Furthermore, with the emerging integration of micro-electromechanical systems (MEMS) technology with HgCdTe-based IR devices [15–17], the ability to complement the versatility of MEMS with a more robust HgCdSe material system holds great promise for achieving a reliable and robust device technology. Since understanding and control of mechanical properties in MEMS structures is critical to achieving reliability, it is essential to determine the mechanical parameters of HgCdSe, in particular the material hardness (H) and Young's modulus (E). However, the available published research on this is very limited in the open literature, especially for MBE-grown HgCdSe epilayers.

Nanoindentation has been widely utilized to investigate the mechanical properties of semiconductor materials [18–24]. By loading and unloading the indenter tip, the response of indented material due to structural deformation can be investigated from the so-called load–displacement (P-h) curves. Furthermore, compared to alternative methods of determining mechanical properties on the basis of MEMS technology [25], nanoindentation does not require elaborate fabrication of diagnostic microstructures [26,27], especially when fabrication processes are yet to be developed for the HgCdSe material system. Therefore, we have adopted nanoindentation to investigate the elasto-plastic properties of MBE-grown $Hg_{1-x}Cd_xSe$ with $x \sim 0.3$ on GaSb (211)B substrates, and present a direct comparison with HgCdTe of the same x-value [21,28]. It is essential to note that the performance of HgCdTe-based detector is severely sensitive to its technological quality due to its soft and brittle character [22]. An IR material with more robust

* Corresponding author at: M018, Dept. EECE, The University of Western Australia, 35 Stirling Highway, 6009 Perth, Australia.
E-mail address: wen.lei@uwa.edu.au (W. Lei).

https://doi.org/10.1016/j.infrared.2022.104446
Received 29 July 2022; Received in revised form 31 October 2022; Accepted 1 November 2022
Available online 13 November 2022

mechanical properties than HgCdTe could provide an attractive alternative for the development of more fabrication-tolerant IR device technologies in the future.

2. Depth sensing indentation

In a typical nanoindentation experiment, a hard diamond indentation tip is applied to the surface of the thin-film specimen. The diamond indenter is initially pressed into the specimen surface with preset loading, and then gradually extracted by controllably removing the loading. During the measurement process, both the loading force (P) and the corresponding displacement of the tip (h) are recorded, allowing deformation information to be logged in the form of a load–displacement (P-h) curve, which is schematically presented in Fig. 1. The loading segment of the P-h curve is associated with the mechanical resistance of the indented material as the tip penetrates, which typically reflects both the elastic and plastic properties of the specimen. When the loading force reaches its peak value, the corresponding penetration depth is labelled as the maximum depth (h_{max}). The unloading segment reflects the recovery process of indented material, which is dominated by the elastic properties of the specimen [29]. If the material is fully elastic, the final penetration depth (h_f) will be zero once all loading is removed, meaning that full recovery of the indented material has occurred. On the other hand, for fully plastic material where no recovery takes place h_f is equal to h_{max}. It should be noted that most materials demonstrate elasto-plastic character, which can be quantitatively determined by the ratio of h_f to h_{max}, which can be extracted from the recorded P-h curves.

2.1. Determination of Young's modulus

Based on the P-h curves, a number of methods can be used to extract the parameters of elastic modulus and hardness [30–33]. In this study, we adopt the most commonly used Oliver and Pharr method [34] to analyse the unloading segments of the P-h curves for determining the Young's modulus and hardness parameters [29,34]. By considering the typical P-h curve as illustrated in Fig. 1, the contact stiffness S between the Berkovich tip and the specimen can be calculated as follows:

$$S = \frac{dP}{dh}, \tag{1}$$

where dP and dh are the differential changes of the loading force and the penetration displacement, respectively. Furthermore, the relationship between P and h in the unloading segment can be described with a power law relationship.

$$P = a(h - h_f)^m, \tag{2}$$

where a and m are the parameters to be fitted. In this study, the unloading segment of the P-h curve is preset to be fitted over the range of 60–90 % of the peak loading value. Combined with Eqs. (1) and (2), the initial slope of the unloading curve can be extracted, which is defined as the contact stiffness (S). The elastic modulus of the specimen is derived from the nanoindentation measurement using the numerical relationship between the contact stiffness (S) and the projected contact area (A_c) [35]:

$$S = \frac{2E_r}{\sqrt{\pi}}\sqrt{A_c}, \tag{3}$$

where E_r is the reduced modulus incorporating both the deformation effect of the indented material and that of the indentation tip. The combined effects can be expressed as:

$$\frac{1}{E_r} = \frac{1 - v_t^2}{E_t} + \frac{1 - v^2}{E}, \tag{4}$$

where E_t and v_t represent the Young's modulus and Poisson ratio of indenter tip, respectively. In our study, a Berkovich diamond tip has been used whose E_t and v_t are 1141 GPa and 0.07, respectively. In Eq. (4) for isotropic materials, E and ν are the Young's modulus and Poisson ratio, and the ratio $\frac{E}{1-\nu^2}$ is recognized as the plain-strain Young's modulus [36]. For anisotropic materials like HgCdSe [37], the value of the measured elastic modulus reflects the effective elastic behaviour of the indented material with contributions from various crystal orientations. Theoretically, for anisotropic materials the value of E should change with different orientations in indented material. However, it is still common practice to apply Eq. (4) to extract the effective elastic modulus, which can generally be treated as the indentation Young's modulus even for anisotropic materials [28].

2.2. Determination of hardness

As indicated in Fig. 1 (a), the projected contact area A_c between the indenter tip and the specimen depends on the shape of the tip and the penetration depth. The parameter illustrating how deep the indenter and specimen are in contact is labeled as the maximum contact depth, h_c. Correspondingly, h_{max} represents the maximum penetration depth

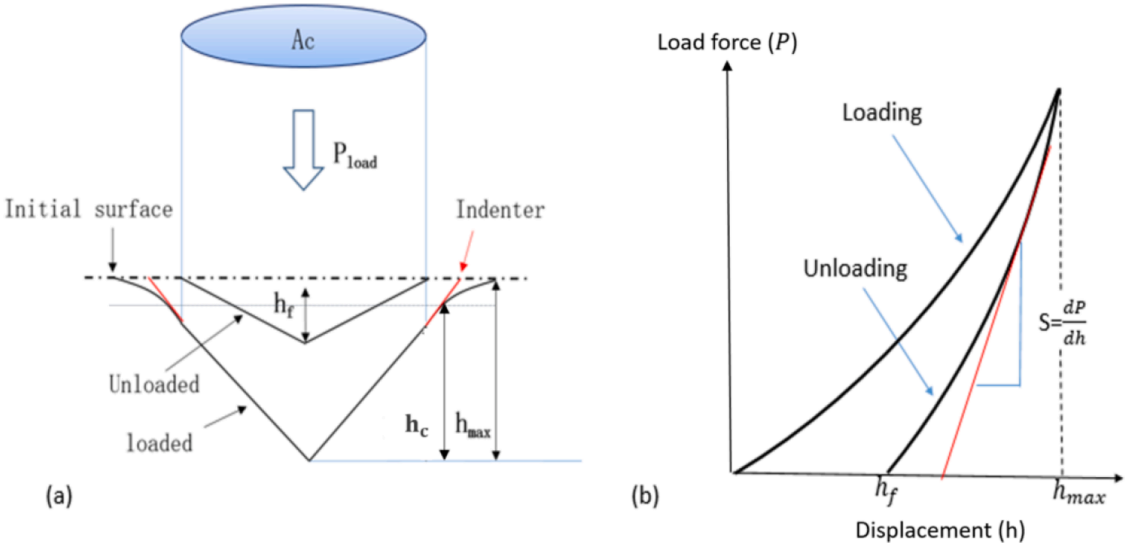

Fig. 1. (a) Schematic nano-indentation process, where A_c is the contact area, h_f is the final depth, and h_{max} is the maximum depth of the penetrating indentation tip; and (b) typical load–displacement (P-h) curve of indentation tip.

under the largest loading force (P_{max}). To relate the penetration displacement of the tip in the specimen with the loading force, the following model is used [38]:

$$h_{max} - h_c = \varepsilon \frac{P_{max}}{S}, \quad (5)$$

where ε is a coefficient related to the shape of the indenter tip. For a Berkovich tip, the suggested ε value is 0.75 [39]. Once the penetration depth is determined, the contact area A_c can be extracted from the tip area function $A_c = f(h_c)$ [34], which needs to be pre-calibrated by using a standard specimen related to tip geometric imperfection and system compliance. Based on the typical definition of hardness (H), we treat H as the mean pressure which the specimen can sustain at a particular loading force. Once the contact area A_c is determined for P_{max}, H can be extracted as follows:

$$H = \frac{P_{max}}{A_c} \quad (6)$$

3. Experimental details

A Brucker TI 950 nanoindentation system combined with a Performech™ Advanced Control Module was used to undertake the measurements on $Hg_{0.7}Cd_{0.3}Se$ epilayers, which were grown to a thickness of approximately 4.5 μm on GaSb (211)B substrates using the Riber 32P MBE at The University of Western Australia. Note that the $Hg_{0.7}Cd_{0.3}Se$ materials studied in this work are of mono-crystalline as indicated by the XRD (X-ray diffraction) rocking curve measurement and long strip RHEED (reflection high-energy electron diffraction) pattern observed during the MBE growth which are shown in Figure S1 of the supplementary material. Multiple indentation points were performed on the surface of $Hg_{0.7}Cd_{0.3}Se$ sample using the Berkovich tip under peak loads ranging from 400 μN to 2000 μN with an increment of 50 μN. The indenter loading function adopted in this study is illustrated in Fig. 2 (a). In this profile, the loading force increases to the maximum loading force (P_{max}) within the first 10 s, then decreases to 10 % of P_{max} in the next 10 s, and then increases to P_{max} in the following 10 s.

Subsequently, the loading force is held at P_{max} for 15 s, and then reduces to 0 over the final 15 s.

The pre-indent and the constant load within the indenter loading function serve the purpose of dissipating the influence on the measurement associated with time-dependent processes within the specimen. The final unloading segment can be regarded to be essentially free of effects associated with time-dependent deformation processes such as material creep, allowing for the extracted Young's modulus and hardness values to be representative of the indented material [40]. Fig. 2 (b) shows an exemplar indentation point on the surface of HgCdSe sample confirming that the Berkovich diamond tip geometry has been well formed on the surface of the investigated sample.

4. Results and discussion

The measured values of Young's modulus (E) and hardness (H) of $Hg_{0.7}Cd_{0.3}Se$ extracted from nanoindentation load–displacement (P-h) curves are displayed in Fig. 3 as a function of contact depth, h_c. Since the maximum penetration depth is less than 250 nm and does not exceed 10 % of the HgCdSe thin film thickness (~4.5μ m), the extracted values of E and H can be considered to be essentially free from any substrate effects [24]. It can be observed in Fig. 3 that the values of E for $Hg_{0.7}Cd_{0.3}Se$ as a function of contact depth have significant variation, and the average value is determined to be ~ 51 GPa with ~ 7.4 GPa standard deviation (σ). This variation is plausibly caused by tip-shape irregularities especially for contact depths less than ~ 100 nm. Note Figure S2 shows the large variation when contact depths are less than ~ 100 nm. Thus only the E values with the contact depths more than ~ 100 nm are used for discussion in this work. However, the 43 indentation points provide a valid database to effectively mitigate this artificial interference. The average value of E for previously reported $Hg_{0.7}Cd_{0.3}Te$ data is found to be ~ 50 GPa [21], which is similar to the average value of E for

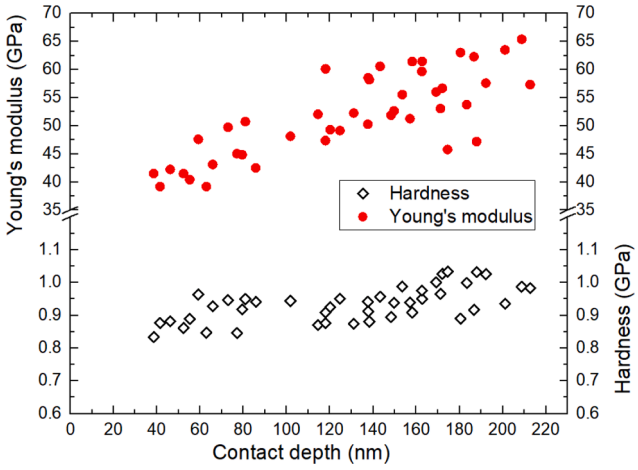

Fig. 3. Measured hardness (open diamonds) and Young's modulus (closed diamonds) of MBE-grown $Hg_{0.7}Cd_{0.3}Se$ thin film as a function of contact depth.

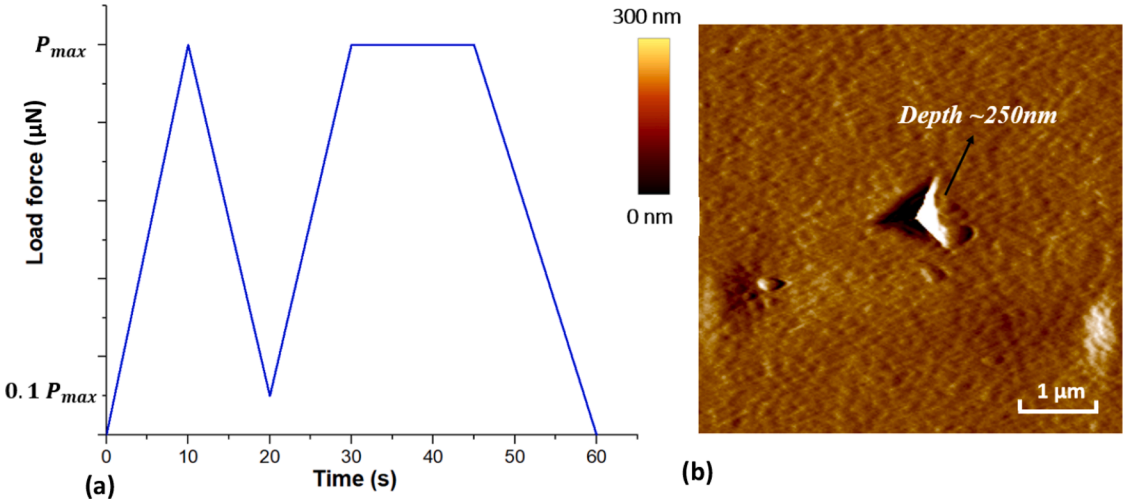

Fig. 2. (a) Indenter load function adopted in this work, and (b) an AFM image of an indentation point on a $Hg_{0.7}Cd_{0.3}Se$ sample.

$Hg_{0.7}Cd_{0.3}Se$, and this similarity is likely to be related to the highly analogous crystal structure between HgCdTe and HgCdSe (both HgCdTe and HgCdSe belong to the IIB-VIA family with zinc-blende structure) [41,42]. On the other hand, the trend as a function of contact depth observed in this study for H of $Hg_{0.7}Cd_{0.3}Se$ differs from the previous observation for $Hg_{0.7}Cd_{0.3}Te$, which included indentations with contact depths extending to 800 nm. The resultant H values for $Hg_{0.7}Cd_{0.3}Te$ obtained below an indentation contact depth of ~ 300 nm were found to increase with decreasing depth, which was attributed to the indentation size effect formulated by the work of Nix and Gao [43]. In contrast, it is evident from Fig. 3 that the measured H values for $Hg_{0.7}Cd_{0.3}Se$ remain constant over the investigated indentation contact depth range of 40–220 nm. Since this indentation depth range is not as extensive in comparison to the previous $Hg_{0.7}Cd_{0.3}Te$ study, we do not discuss extensively the noted differences. Nevertheless, since the indentation size effect is expected to be especially pronounced in relatively soft crystalline materials, the lack of an observed trend in $Hg_{0.7}Cd_{0.3}Se$ supports the notion that HgCdSe is not such soft in comparison to HgCdTe. The data for the observed $Hg_{0.7}Cd_{0.3}Se$ hardness gave an average value of H ~ 0.93 GPa with σ ~ 0.05 GPa, which can be considered to be notably greater than the average value of H ~ 0.66 GPa found for $Hg_{0.7}Cd_{0.3}Te$ [21]. This could be associated with Cd-Se (111.3 kcal/mol) and Hg-Se (110.2 kcal/mol) bonds having larger cohesive energies than those of Cd-Te (95.4 kcal/mol) and Hg-Te (94.2 kcal/mol) [44]. Considering that HgCdTe has always been considered a soft-brittle material leading to severe constraints on its fabrication technology, HgCdSe with a larger hardness value may therefore be a more robust option from the point of view of tolerance to fabrication processes.

To further investigate the elasto-plastic behaviour of $Hg_{0.7}Cd_{0.3}Se$, we focus our attention on the details of the recorded P-h curves. Fig. 4(a) illustrates the load-penetration curves of $Hg_{0.7}Cd_{0.3}Se$ epilayers for multiple peak load forces, P_{max}, ranging from 100 to 300 μN. For P_{max} less than or equal to 150 μN, the loading and unloading segments of the curves overlap fully with one another, indicating that the indented material presents completely elastic behaviour. For greater values of P_{max}, the $Hg_{0.7}Cd_{0.3}Se$ presents an elasto-plastic response with typical discontinuities observable in the penetration depth, which are generally referred to as "pop- in" events [45].

The "pop-in" events have previously been linked with rapid nucleation and propagation of homogenous dislocations [46], the occurrence of cracks and slippage in crystals [47], and the onset of phase transformations [48]. From similar studies on silicon [48], the onset of phase transformation is strongly linked with the occurrences of obvious discontinuities in the unloading segments, which are commonly referred to as "pop-out" events. However, as indicated in Fig. 4, no "pop-out" events were observed in our experiments. In addition, no evidence of cracking has been observed with any of the indents. Therefore, the onset of plastic deformation and dislocation nucleation in HgCdSe is the most plausible explanation for the occurrence of the observed "pop-in" events, which is also consistent with the conclusion obtained in a previous study on HgCdTe (more details are discussed later in this work) [28].

Several studies in the open literature have demonstrated that the critical shear stress required for initiation of homogenous nucleation of dislocations and the onset of plastic flow, τ_c, can be approximated by [49–51]:

$$\tau_c \approx \frac{G}{10}, \tag{7}$$

where G is the shear modulus of the material. For $Hg_{0.7}Cd_{0.3}Se$, the shear modulus can be interpolated using Vegard's Law based on the theoretical shear modulus of HgSe and CdSe [52,53]. Using this approach, the theoretical critical shear stress required to induce homogeneous nucleation of dislocations in $Hg_{0.7}Cd_{0.3}Se$ can be estimated to be 2.25 GPa. On the other hand, the maximum shear stress, τ_T, for a spherical indenter under fully elastic contact conditions with R ≫ h can be expressed as a function of the average contact pressure, p_m, as [54]:

$$\tau_T \approx 0.465 p_m \approx 0.465 \frac{P}{A_c} \approx 0.465 \frac{P}{\pi R h}, \tag{8}$$

where P, A_c, R and h represent the load force applied to the indenter, projected area, radius of indentation tip, and penetration depth, respectively. Because the Berkovich indentation tip used in our study is not perfectly sharp and is effectively rounded, Eq. (8) can be applied to the range of shallow indentations undertaken in this study with the indenter tip radius, R, estimated to be around 700 nm, by applying Hertzian elastic equations [55] to the fully elastic P-h curves.

Table 1 compares the theoretical critical shear stress required to induce homogenous nucleation of dislocations, τ_c, and the maximum shear stress induced by the indenter immediately prior to the onset of a "pop-in" event, τ_T. The range of τ_T represents the values obtained from the P-h curves with a "pop-in" event occurring. To provide a direct comparison between τ_c and τ_T, the percentage of τ_c that τ_T has achieved just before a "pop-in" event is also listed in Table 1. It is evident from these values that τ_T developed immediately prior to the occurrence of a "pop-in" event is well correlated with the theoretically calculated τ_c using the elastic constants for perfect single-crystal HgCdSe, suggesting that "pop-in" events in $Hg_{0.7}Cd_{0.3}Se$ are linked with homogenous nucleation of dislocations and the onset of plastic deformation. Similar findings have also been found for MBE-grown $Hg_{0.7}Cd_{0.3}Te$ epilayers

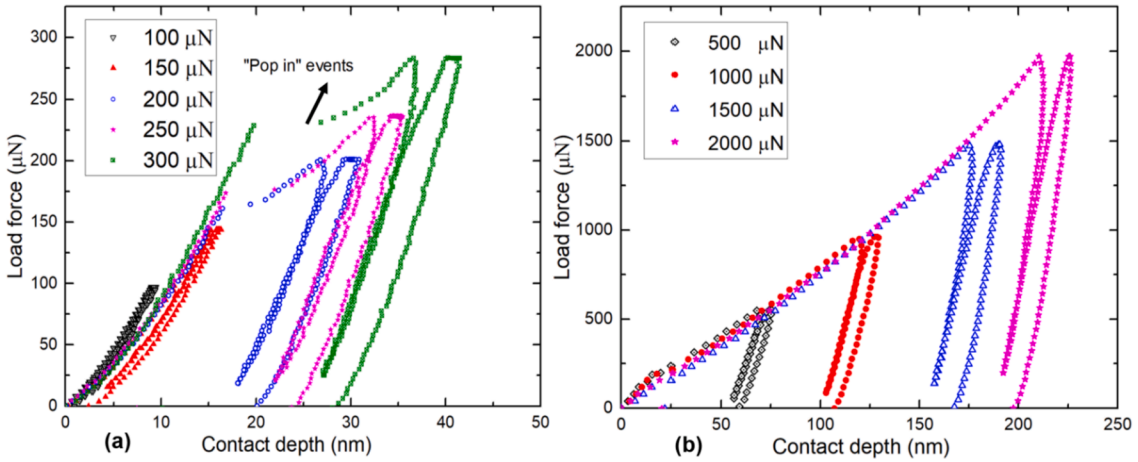

Fig. 4. (a) The load-penetration (P-h) curves for $Hg_{0.7}Cd_{0.3}Se$ with $\boldsymbol{P_{max}}$ ranging from 100 to 300 μN in 50 μN increments. The characteristic discontinuities or "pop-in" events are labelled with an arrow. (b) P-h curves for $Hg_{0.7}Cd_{0.3}Se$ with much larger $\boldsymbol{P_{max}}$ ranging from 500 to 2000 μN in 500 μN increments. Notably no discontinuities are observed for the unloading segments.

Table 1
Data extracted from nanoindentation measurements on MBE-grown $Hg_{0.7}Cd_{0.3}Se$ epilayers in comparison to data for $Hg_{0.7}Cd_{0.3}Te$ taken from Ref [21] (E, average Young's modulus; H, average hardness; τ_c, theoretical critical shear stress; τ_T, maximum shear stress induced by indentation load force immediately prior to a "pop-in" event).

	Thickness (um)	E (GPa)	H (GPa)	τ_c(GPa)	τ_T(GPa)	τ_T/τ_c(%)
$Hg_{0.7}Cd_{0.3}Se$	4.5	51	0.93	2.25	2.06–2.43	92–108
$Hg_{0.7}Cd_{0.3}Te$	10	50	0.66	1.80	1.70–1.80	94–101

[21]. As shown in Ref.21, plastic deformation happened when the maximum shear stress (τ_T) induced by the indenter immediately prior to the "pop-in" event was greater than the theoretically critical shear stress (τ_c) required to induce homogeneous nucleation of dislocations, and the onset of plastic deformation was postulated to be associated with the homogenous nucleation and propagation of dislocations. The value of τ_c can, to some extent, reflect the limiting elastic stress above which irreversible plastic deformation will be generated. Table 1 compares the values of τ_c for $Hg_{0.7}Cd_{0.3}Se$ and $Hg_{0.7}Cd_{0.3}Te$, and it is evident that the shear stress for the onset of plastic deformation for $Hg_{0.7}Cd_{0.3}Se$ material is significantly greater than for $Hg_{0.7}Cd_{0.3}Te$.

The elasto-plastic character of $Hg_{0.7}Cd_{0.3}Se$ can be quantitively evaluated by the ratio of h_f to h_{max}, where h_{max} represents the maximum penetration depth during loading and h_f is the final depth after the indented material recovers from the unloading process. The value of h_f/h_{max} ranges from 0 for purely elastic materials, to 1 for purely plastic materials. This parameter is plotted in Fig. 5 for our experiments as a function of indentation contact depth, and is directly compared to the data determined previously for $Hg_{0.7}Cd_{0.3}Te$. It is evident that for penetration depths less than 15 nm, $Hg_{0.7}Cd_{0.3}Se$ epilayers tend to display a high degree of elastic character (h_f/h_{max} less than 0.2). This agrees well with the observations from Fig. 4, where "pop-in" events are found to occur for a contact depth of approximately 15 nm. It can also be observed from Fig. 5 that for increasing penetration depths beyond the "pop-in" event depth, the value of h_f/h_{max} continues to rapidly increase and then subsequently saturates, reaching a value of 0.83 for contact depths exceeding 100 nm. The rapid increase of h_f/h_{max} in Fig. 5 indicates that there is a sharp transition from elastic to plastic character in both $Hg_{0.7}Cd_{0.3}Te$ and $Hg_{0.7}Cd_{0.3}Se$ material with increasing contact depth, which occurs close to the depth of "pop-in" events. This is consistent with the notion that plastic deformation in HgCdSe is associated with homogenous nucleation of dislocations and their propagation.

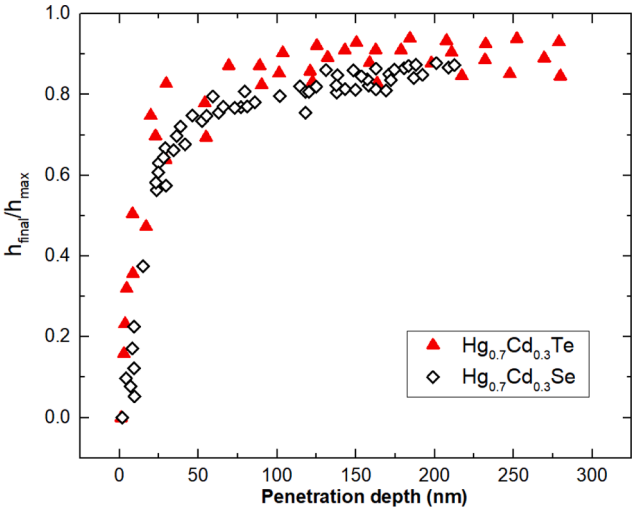

Fig. 5. The measured ratio of final penetration depth, h_{final}, to the maximum indentation depth, h_{max}, as a function of penetration depth for $Hg_{0.7}Cd_{0.3}Se$ (open diamonds) and $Hg_{0.7}Cd_{0.3}Te$ (full triangles). The HgCdTe data is taken from Ref [21].

5. Summary and conclusions

In this paper, the elasto-plastic properties of MBE-grown $Hg_{0.7}Cd_{0.3}Se$ thin films on GaSb (211)B substrate have been determined via the nanoindentation technique. The Young's modulus and hardness of $Hg_{0.7}Cd_{0.3}Se$ epilayers have been determined to be approximately 51 (with $\sigma \sim 7.4$) GPa and 0.93 (with $\sigma \sim 0.05$) GPa, respectively. Load-penetration curves indicate that for increasing indentation load there is a transition from purely elastic to the elasto-plastic character in HgCdSe, and this transition is marked by characteristic "pop-in" discontinuities. The maximum shear stress, τ_T, induced by the indenter just prior to a "pop-in" event agrees well with the critical shear stress, τ_c, required to induce homogenous dislocation nucleation calculated using the elastic constants for ideal single-crystal $Hg_{0.7}Cd_{0.3}Se$, indicating that the plastic deformation associated with a "pop-in" event in $Hg_{0.7}Cd_{0.3}Se$ is linked to the homogenous nucleation and propagation of dislocations.

$Hg_{0.7}Cd_{0.3}Se$ is found to have greater hardness and shear strength in comparison to $Hg_{0.7}Cd_{0.3}Te$, which is potentially correlated to the larger cohesive energy of Cd-Se and Hg-Se bonds in comparison to Cd-Te and Hg-Te bonds [44]. Even though HgCdTe-based infrared detectors have dominated the high-performance end of the aerospace and defence market for many decades, the soft-brittle nature continues to present significant challenges for conventional manufacturing processes in terms of production yield and cost. With comparable infrared optical parameters to HgCdTe [11,13,14,56], HgCdSe possesses more favourable hardness and elastic shear strength, and thus presents a potential pathway to increase the tolerance to fabrication processes, in particular towards potential integration of infrared sensors with MEMS technologies.

Declaration of Competing Interest

The authors declare that they have no known competing financial interests or personal relationships that could have appeared to influence the work reported in this paper.

Data availability

Data will be made available on request.

Acknowledgments

This work was supported by the Australian Research Council (DP200103188, DP170104562, CE200100010, and LE170100233). Facilities used in this work are supported by the WA node of the Australian National Fabrication Facility (ANFF), and the Centre for Microscopy, Characterization and Analysis (CMCA) at UWA.

References

[1] W. Lei, J. Antoszewski, L. Faraone, Progress, challenges, and opportunities for HgCdTe infrared materials and detectors, Appl Phys Rev 2 (2015), 041303.
[2] P. Norton, HgCdTe infrared detectors, Optoelectronics review 10 (2002) 159–174.
[3] W. Hu, X. Chen, Z. Ye, W. Lu, A hybrid surface passivation on HgCdTe long wave infrared detector with in-situ CdTe deposition and high-density hydrogen plasma modification, Applied Physics Letters 99 (2011), 091101.

[4] J. He, Q. Li, P. Wang, F. Wang, Y. Gu, C. Shen, M. Luo, C. Yu, L. Chen, X. Chen, Design of a bandgap-engineered barrier-blocking HOT HgCdTe long-wavelength infrared avalanche photodiode, Opt Express 28 (2020) 33556–33563.

[5] Q. Li, R. Xie, F. Wang, S. Liu, K. Zhang, T. Zhang, Y. Gu, J. Guo, T. He, Y. Wang, SRH suppressed PGI design for very long-wavelength infrared HgCdTe photodiodes, Opt Express 30 (2022) 16509–16517.

[6] W. Lei, R. Gu, J. Antoszewski, J. Dell, L. Faraone, GaSb: a new alternative substrate for epitaxial growth of HgCdTe, J Electron Mater 43 (2014) 2788–2794.

[7] W. Lei, R.J. Gu, J. Antoszewski, J. Dell, G. Neusser, M. Sieger, B. Mizaikoff, L. Faraone, MBE Growth of Mid-wave Infrared HgCdTe Layers on GaSb Alternative Substrates, J Electron Mater 44 (2015) 3180–3187.

[8] W. Lei, Y.L. Ren, I. Madni, L. Faraone, Low dislocation density MBE process for CdTe-on-GaSb as an alternative substrate for HgCdTe growth, Infrared Phys Techn 92 (2018) 96–102.

[9] W. Pan, R. Gu, Z. Zhang, J. Liu, W. Lei, L. Faraone, Strained CdZnTe/CdTe superlattices as threading dislocation filters in lattice mismatched MBE growth of CdTe on GaSb, J Electron Mater 49 (2020) 6983–6989.

[10] K. Doyle, C.H. Swartz, J.H. Dinan, T.H. Myers, G. Brill, Y.P. Chen, B.L. VanMil, P. Wijewarnasuriya, Mercury cadmium selenide for infrared detection, J Vac Sci Technol B 31 (2013) 03C124.

[11] W.W. Pan, Z.K. Zhang, W. Lei, Z. Liu, L. Faraone, A Raman spectroscopy study of MBE-grown Hg1-xCdxSe alloys grown on GaSb (211) by molecular beam epitaxy, Infrared Phys Techn 97 (2019) 365–370.

[12] W. Pan, Z. Zhang, W. Lei, L. Faraone, Optical Properties of MBE-Grown Hg 1–x Cd x Se, J Electron Mater (2019) 1–6.

[13] Z.K. Zhang, W.W. Pan, J.L. Liu, W. Lei, A review on MBE-grown HgCdSe infrared materials on GaSb (211)B substrates, Chinese Phys B 28 (2019), 018103.

[14] W. Lei, Y.L. Ren, I. Madni, G.A. Umana-Membreno, L. Faraone, MBE growth of high quality HgCdSe on GaSb substrates, Infrared Phys Techn 92 (2018) 197–202.

[15] J. Antoszewski, K.J. Winchester, T. Nguyen, A.J. Keating, K.D. Silva, C.A. Musca, J. M. Dell, L. Faraone, Materials and processes for MEMS-based infrared microspectrometer integrated on HgCdTe detector, Ieee J Sel Top Quant 14 (2008) 1031–1041.

[16] D.A. Kozak, B. Fernandez, S. Velicu, J. Kubby, Prototyping of MWIR MEMS-based optical filter combined with HgCdTe Detector, in: MOEMS and Miniaturized Systems IX, International Society for Optics and Photonics, 2010, p. 75940W.

[17] P. Mitra, J. Beck, M. Skokan, J. Robinson, J. Antoszewski, K. Winchester, A. Keating, T. Nguyen, K. Silva, C. Musca, Adaptive focal plane array (AFPA) technologies for integrated infrared microsystems, in: Intelligent Integrated Microsystems, International Society for Optics and Photonics, 2006, pp. 62320G.

[18] Z. Zhang, H. Gao, W. Jie, D. Guo, R. Kang, Y. Li, Chemical mechanical polishing and nanomechanics of semiconductor CdZnTe single crystals, Semicond Sci Tech 23 (2008), 105023.

[19] K. Wasmer, R. Gassilloud, J. Michler, C. Ballif, Analysis of onset of dislocation nucleation during nanoindentation and nanoscratching of InP, J Mater Res 27 (2012) 320–329.

[20] A.C. Fischer-Cripps, Contact mechanics, in: Nanoindentation, Springer, New York, 2004, pp. 1-20.

[21] M. Martyniuk, R.H. Sewell, C.A. Musca, J.M. Dell, L. Faraone, Nanoindentation of HgCdTe prepared by molecular beam epitaxy, Applied Physics Letters 87 (2005), 251905.

[22] H.X. Zhou, S. Qiu, X.Z. Zhang, C.G. Xu, Mechanical characteristics of soft-brittle HgCdTe single crystals investigated using nanoindentation and nanoscratching, Appl Surf Sci 258 (2012) 9756–9761.

[23] Y. Li, R.K. Kang, H. Gao, J.H. Wang, Y.J. Lang, Nanomechanical behaviors of (110) and (111) CdZnTe crystals investigated by nanoindentation, Rare Metals 28 (2009) 570–575.

[24] Y.-G. Jung, B.R. Lawn, M. Martyniuk, H. Huang, X.Z. Hu, Evaluation of elastic modulus and hardness of thin films by nanoindentation, J Mater Res 19 (2004) 3076–3080.

[25] B.A. Walmsley, J.M. Dell, Y. Liu, X.Z. Hu, M.B. Bush, L. Faraone, Design and optimisation of a MEMS-based tunable Fabry-Pérot infrared filter, in: In: 2006 Conference on Optoelectronic and Microelectronic Materials and Devices, IEEE, 2006, pp. 272–275.

[26] K.L. Brookshire, R. Rafiei, M. Martyniuk, K. Silva, L. Faraone, Y. Liu, Investigation of thermal expansion effects on Si-based MEMS structures, J Microelectromech S 25 (2016) 549–556.

[27] M. Martyniuk, J. Antoszewski, C. Musca, J. Dell, L. Faraone, Stress in low-temperature plasma enhanced chemical vapour deposited silicon nitride thin films, Smart Materials and Structures 15 (2005) S29.

[28] M. Martyniuk, R.H. Sewell, C.A. Musca, J.M. Dell, L. Faraone, Determination of HgCdTe elasto-plastic properties using nanoindentation, J Electron Mater 35 (2006) 1197–1205.

[29] W.C. Oliver, G.M. Pharr, Measurement of hardness and elastic modulus by instrumented indentation: Advances in understanding and refinements to methodology, J Mater Res 19 (2004) 3–20.

[30] M. Doerner, D. Gardner, W. Nix, Plastic properties of thin films on substrates as measured by submicron indentation hardness and substrate curvature techniques, J Mater Res 1 (1986) 845–851.

[31] S. Bulychev, V. Alekhin, M.K. Shorshorov, A. Ternovskii, Mechanical properties of materials studied from kinetic diagrams of load versus depth of impression during microimpression, Strength of Materials 8 (1976) 1084–1089.

[32] J. Gubicza, A. Juhász, J. Lendvai, A new method for hardness determination from depth sensing indentation tests, J Mater Res 11 (1996) 2964–2967.

[33] M. Sakai, Energy principle of the indentation-induced inelastic surface deformation and hardness of brittle materials, Acta Metall Mater 41 (1993) 1751–1758.

[34] W.C. Oliver, G.M. Pharr, An improved technique for determining hardness and elastic modulus using load and displacement sensing indentation experiments, J Mater Res 7 (1992) 1564–1583.

[35] C.-M. Cheng, Y.-T. Cheng, On the initial unloading slope in indentation of elastic-plastic solids by an indenter with an axisymmetric smooth profile, Applied physics letters 71 (1997) 2623–2625.

[36] K.M. Knowles, The plane strain young's modulus in cubic materials, Journal of Elasticity 128 (2017) 147–173.

[37] I. Madni, G.A.U. Membreno, W. Lei, L. Faraone, Investigation of MBE-Growth of Mid-Wave Infrared Hg1-xCdxSe, J Electron Mater 47 (2018) 5691–5698.

[38] I.N. Sneddon, The relation between load and penetration in the axisymmetric Boussinesq problem for a punch of arbitrary profile, International journal of engineering science 3 (1965) 47–57.

[39] G. Pharr, A. Bolshakov, Understanding nanoindentation unloading curves, J Mater Res 17 (2002) 2660–2671.

[40] A. Ngan, B. Tang, Viscoelastic effects during unloading in depth-sensing indentation, J Mater Res 17 (2002) 2604–2610.

[41] W.F. Zhao, G. Brill, Y. Chen, D.J. Smith, Microstructural Characterization of HgCdSe Grown by Molecular Beam Epitaxy on ZnTe/Si(112) and GaSb(112) Substrates, J Electron Mater 41 (2012) 2852–2856.

[42] R. Nelmes, M. McMahon, Structural transitions in the group IV, III-V, and II-VI semiconductors under pressure, in: Semiconductors and semimetals, Elsevier, 1998, pp. 145-246.

[43] W.D. Nix, H. Gao, Indentation size effects in crystalline materials: a law for strain gradient plasticity, Journal of the Mechanics and Physics of Solids 46 (1998) 411–425.

[44] A. Verma, B. Sarkar, V. Jindal, Cohesive energy of zincblende (AIIIBV and AIIBVI) structured solids, Pramana 74 (2010) 851–855.

[45] G. Zhang, Z. Wei, R.E. Ferrell, S. Guggenheim, R.T. Cygan, J. Luo, Evaluation of the elasticity normal to the basal plane of non-expandable 2: 1 phyllosilicate minerals by nanoindentation, American Mineralogist 95 (2010) 863–869.

[46] D.F. Bahr, D. Kramer, W. Gerberich, Non-linear deformation mechanisms during nanoindentation, Acta Mater 46 (1998) 3605–3617.

[47] P. Feltham, R. Banerjee, Theory and application of microindentation in studies of glide and cracking in single crystals of elemental and compound semiconductors, Journal of materials science 27 (1992) 1626–1632.

[48] B. Haberl, J. Bradby, M. Swain, J. Williams, P. Munroe, Phase transformations induced in relaxed amorphous silicon by indentation at room temperature, Applied physics letters 85 (2004) 5559–5561.

[49] J. Pethica, D. Tabor, Contact of characterised metal surfaces at very low loads: Deformation and adhesion, Surf Sci 89 (1979) 182–190.

[50] R.C. Thomas, J. Houston, T.A. Michalske, R.M. Crooks, The mechanical response of gold substrates passivated by self-assembling monolayer films, Science 259 (1993) 1883–1885.

[51] T. Michalske, J. Houston, Dislocation nucleation at nano-scale mechanical contacts, Acta Mater 46 (1998) 391–396.

[52] N. Kishore, V. Nagarajan, R. Chandiramouli, Mechanical properties and band structure of CdSe and CdTe nanostructures at high pressure-a first-principles study, Processing and Application of Ceramics 13 (2019) 124–131.

[53] I. Düz, İ. Erdem, S. Özdemir Kart, V. Kuzucu, First principles investigations of HgX (X= S, Se and Te), Archives of, Materials Science and Engineering 79 (2016) 5–11.

[54] D. Lorenz, A. Zeckzer, U. Hilpert, P. Grau, H. Johansen, H. Leipner, Pop-in effect as homogeneous nucleation of dislocations during nanoindentation, Physical review B 67 (2003), 172101.

[55] A. Fischer-Cripps, The Hertzian contact surface, Journal of materials science 34 (1999) 129–137.

[56] W. Pan, Z. Zhang, W. Lei, L. Faraone, Optical Properties of MBE-Grown Hg 1–x Cd x Se, J Electron Mater 48 (2019) 6063–6068.